Received May 10, 2021, accepted June 12, 2021, date of publication June 15, 2021, date of current version June 28, 2021.

Digital Object Identifier 10.1109/ACCESS.2021.3089582

Highly Efficient Front End Direct Conversion Receiver for 28-GHz Wireless Access Point

MOHAMMAD AKBARI[1], (Member, IEEE), MOHAMMADMAHDI FARAHANI[2], (Member, IEEE), MANSOOR DASHTI ARDAKANI[3], ALI LALBAKHSH[4], (Member, IEEE), SAMAN ZARBAKHSH[2], (Member, IEEE), SERIOJA OVIDIU TATU[3], (Senior Member, IEEE), ABDEL-RAZIK SEBAK[2], (Life Fellow, IEEE), OMAR M. RAMAHI[5], (Fellow, IEEE), AND TAYEB A. DENIDNI[3], (Fellow, IEEE)

[1]Department of Electrical and Computer Engineering, McMaster University, Hamilton, ON L8S 4K1, Canada
[2]Department of Electrical and Computer Engineering, Concordia University, Montreal, QC H3G 1M8, Canada
[3]National Institute of Scientific Research (INRS-EMT), Montreal, QC H5A 1K6, Canada
[4]School of Engineering, Macquarie University, Sydney, NSW 2109, Australia
[5]Department of Electrical and Computer Engineering, University of Waterloo, Waterloo, ON N2L 3G1, Canada

Corresponding author: Mohammad Akbari (akbari.telecom@gmail.com)

This work was supported in part by the Fonds de recherche du Quebec-Nature et Technologies of Canada (FRQNT), in part by the National Science Engineering Research Council of Canada (NSERC), and in part by the Macquarie University Research Fellowship (MQRF) Fund.

ABSTRACT The manuscript presents the design and characterization of a wideband front-end receiver, based on hollow waveguide technology, for the wireless access point (WAP) applications. The Ka-band receiver is comprised of a low-loss beam-switching antenna network (BSAN) with two-dimensional (2D) scanning property. For demodulation, the receiver uses an efficient six-port network (SPN) that is composed of four 90° hybrid couplers and a 90° phase shifter. To suppress the phase imbalance on the entire band of interest, 27 GHz to 33 GHz, a frequency-independent phase shifter with a minimum phase error is suggested. The SPN receiver is integrated with antenna-in-package in waveguide technology to decrease the insertion losses and noise levels at the first stages. To determine the SPN phase errors, a theoretical and experimental analysis of real-time wireless data transmission utilizing phase-shift keying (PSK) and quadrature amplitude modulated (QAM) signal is conducted. Besides, channel capacity along with beamformer influence on channel performance improvement are determined.

INDEX TERMS Antenna array, beam-switching antenna network (BSAN), direct modulation, homodyne receiver, phase-shift keying (PSK), six port network (SPN), wireless access point (WAP).

I. INTRODUCTION

The exponential extension in the number of users in wireless communication systems, the importance of broad bandwidth (BW) as well as higher data transfer rates, all have recently resulted in the growing request of multimedia services and mobile internets, especially for the upcoming fifth-generation (5G) communication systems [1]–[6]. A Local Multipoint Distribution Service (LMDS) system is capable of offering subscribers a variety of one- and two-way broadband services, such as video programming distribution; video teleconferencing; wireless local loop telephony; and high-speed data transmission, e.g., internet access over 27.500 GHz–28.350 GHz, 29.100 GHz–29.250 GHz, and 31.075 GHz–31.225 GHz bands [6]. A wireless access point (WAP) is a networking hardware device that creates a wireless local area network (WLAN), usually in an office or large building. A WAP connects to a wired router or switch, through an Ethernet cable, and projects a Wi-Fi signal to the desired region (see Fig.1). In addition, the WAP, is able to manage more than sixty simultaneous connections individually [7]. By installing the WAPs throughout the office, users can roam freely from room to room without experiencing network interruptions [7]. One of the considerable problems in the mmWave communication systems, namely 27 GHz – 33 GHz here, is related to free-space propagation loss. To overcome this problem, implementing a high sensitivity receiver using a high-efficiency low-loss

The associate editor coordinating the review of this manuscript and approving it for publication was Tutku Karacolak.

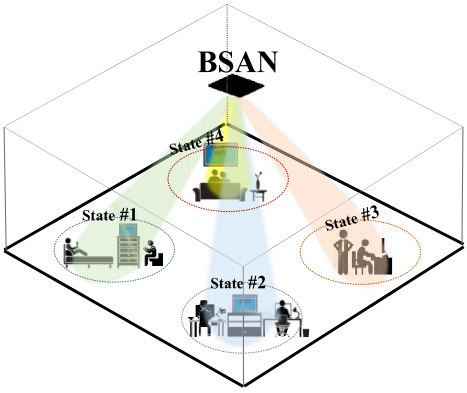

FIGURE 1. Application of the proposed BSAN (beam-switching antenna network) for the wireless access point (WAP).

transmission line can be considered as a critical alternative. Due to some reasons such as the multiuser systems, large channel capacity with wide scanning coverage, as well as high-power efficiency, the existence of intelligent subsystems sounds valuable. The intelligent subsystems are usually divided into two groups: adaptive arrays and beam switching antenna networks (BSAN). However, because of the complex configuration and redundant signal processing, implementing the first group, adaptive arrays, would be costly. Alternatively, because of not using digital controllers, BSAN is realized as an inexpensive approach at the cost of a larger size [8]. The BSANs are developed with diverse configurations, such as the Butler matrix (BM) [8], Blass matrices [9], Rotman lenses [10], and the Nolen matrix [11]. The BM in comparison with others is considered as an uncomplicated and low-priced structure that can be embedded in a small number of components. In the conventional BM, the employment of the 45° phase shifter and crossover coupler are mandatory, which leads to geometrical complexity and performance degradation [8]–[12]. Point out that the crossover is usually implemented utilizing two 3-dB cascaded hybrid couplers, which raise the losses and increase the size considerably [12], [13]. Thus, in terms of complexity, size, bandwidth, losses, and phase errors, the implementation of a BM topology without the crossover coupler and phase shifter is realized as a substantial benefit [8]. Regarding some major factors such as reducing circuit complexity and enabling a higher level of circuit integration than conventional heterodyne receivers, direct-conversion (zero-IF) receivers play a substantial role in the wireless communications [14]. Six-port network (SPN) has been one of the popular topologies that is extensively employed in zero-IF receivers [15], [16]. The initial idea of the use of a six-port topology to study the phase of a microwave signal was introduced in 1964 by Cohn and Weinhouse [17], and expanded by Engen and Hoer [18], [19] in order to precisely measure the complex reflection coefficient in microwave network analysis [19].

In terms of the SPN application, there are two general perspectives. Firstly, the measurement perspective as a reflectometer and the second one as a direct conversion receiver for wireless communications. Both methods take advantage of simplicity and accurately retrieving the magnitude and phase of a complex-valued signal [20]. In 1994, the six-port concept was first introduced as a communications receiver [21]. Simply, the SPN might be realized as a black box including two inputs and four outputs. In addition, the output ports are terminated with power detectors. Characteristic relation or correlation between two input signals (phase and amplitude) can be examined once the relation between the input and output ports are known. The only requirements are that the six-port circuitry is linear and that the outputs are nonlinearly dependent on each other. The four unknowns are achieved from a few characteristic equations [14].

Generally, the six-port reflectometer is calibrated with known test devices such as a sliding load [22]. However, this can never be easy in practice, namely for the short-distance radar systems such as an autonomous cruise control system or a high-precision ranging system.

The reason is that the calibration takes considerable time so that multiple standards should be satisfied to calibrate each port [23]. The dynamic dc-offset voltage is considered as one of main drawbacks of zero-IF receivers that cannot be fully canceled out with respect to the calibration. Correspondingly, the mismatches of the diode characteristics along with the phase errors in a broadband SPN cannot be omitted because it considerably degrades the performance of the receiver system, particularly in terms of bit error rate (BER).

This manuscript represents a broadband highly efficient receiver for WAP application using hollow waveguide technology as a guiding system. The receiver consists of a low-loss wideband BSAN with the capability of 2D scanning. The proposed BSAN is fed by four standard waveguides WR-28 as the input ports, which by different transitions are connected to the 2×2 open-ended waveguide antenna array. Waveguide technologies can support propagation with lower losses at mmWave bands. The focus of the project is to provide an integrated SPN receiver with antennas and the BSAN in waveguide technology to eliminate possible transitions in the first stages, and decrease the insertion losses and noise levels. Implementing broadband and greatly efficient SPN is considered as another contribution here. The proposed SPN is comprised of a combination of four 90° hybrid couplers and of a 90° phase shifter, which is experimentally characterized and validated for signal quadrature down-conversion. To reduce the phase imbalance on the entire band of interest, 27 GHz – 33 GHz, a new phase shifter is represented with the least phase error instead of the use of the conventional delay line with the narrow band property. In addition, a theoretical and experimental analysis of real-time wireless data transmission utilizing phase-shift keying (PSK) and quadrature amplitude modulated (QAM) signal is effectively performed. It is realized that how much the phase errors raised by the 90° phase shifter and 90° hybrid coupler might affect the broadband receiver system performance in terms of time response of pulses.

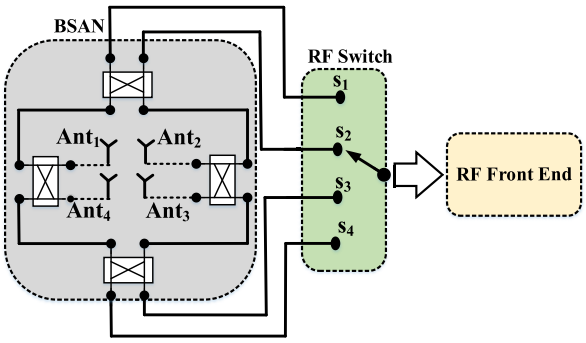

FIGURE 2. General sketch of the 4 × 4 BSAN including four inputs connected to RF switch and four outputs as radiating antenna elements.

II. BEAM-SWITCHING ANTENNA NETWORK (BSAN)

The topology of a 4 × 4 BSAN with the capability of 2D scanning is demonstrated in Fig. 2. The BSAN is comprised of four 3-dB wideband and efficient 90° directional couplers. The BSAN employed here does not use the phase shifter and crossover coupling [8].

The radiating part of the BSAN employs 2 × 2 open-ended waveguide antennas to achieve a 360° lateral scan in 90° steps. In addition, the RF switch, namely SP4T, enables electronic scanning of the array main beam by connecting one of the inputs of the BSAN to the transceiver [24]. Note that the behavior of this kind of BSAN is fully determined in [8]. Referring to the topology depicted in Fig. 2, the 4 × 4 BSAN is comprised of four 3-dB 90° couplers. Basically, cascading two or several sections and properly selecting the impedances of the main and the coupled lines results in a wideband hybrid coupler [25], [26]. The reason for being the narrow bandwidth in a single hybrid coupler is based on the quarter-wavelength lines. However, the type of guiding technology is inherently considered as another main factor of bandwidth matter. As aforementioned, the guiding technology employed in this paper has been hollow waveguide. The coupler is composed of two hollow waveguides with a coupling aperture in the common wall and two distracting appendages (see Fig. 3(a)).

$$(\beta_1 - \beta_2) \times \frac{d_2}{2} = \frac{\pi}{4} \tag{1}$$

Using the approach presented in [26], [27], the coupler performance could be determined. Correspondingly, the coupler is excited with the TE10 mode, however, the high order mode of TE20 can be observed in the coupling region. As shown in Fig. 3(b) and respecting (1), by exciting port P1, the received signals at ports P2 and P3 can be as $\cos((\beta 1 - \beta 2) \times d2/2)$ and $\sin((\beta 1 - \beta 2) \times d2/2)$, respectively. It is notable that $\beta 1$ and $\beta 2$ are referred to as the propagation constants with respect to TE10 and TE20 modes, respectively. Hence, the dimensions for the coupler is achieved by [26]. In addition, due to the existence of high order modes, the simulation optimization is strongly recommended. Ultimately, the optimized dimensions are given in the caption of Fig. 3. Fig. 4 exhibits the numerical results of the scattering parameters along with the

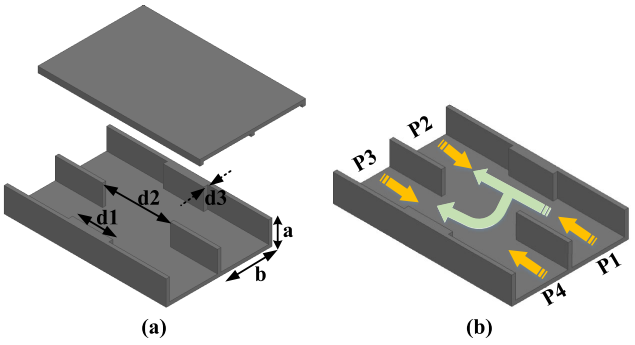

FIGURE 3. Proposed coupler composed of two hollow waveguides with a coupling aperture in the common wall and two distracting appendages. (d1 = 6mm, d2 = 10.1 mm, d3 = 0.6 mm, a = 3.56 mm, and b = 7.11 mm). (a) design of the proposed coupler and (b) the sketch of input ports.

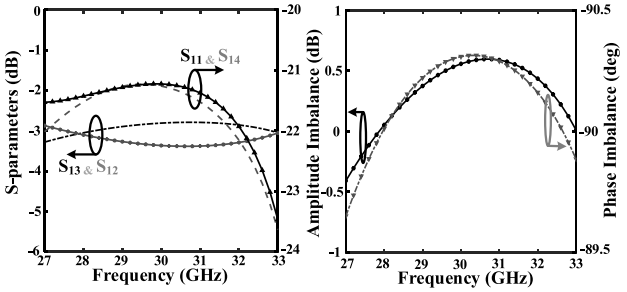

FIGURE 4. (a) Frequency response of the s-parameters belonged to the proposed hybrid coupler and (b) the amplitude and phase imbalance response of the proposed hybrid coupler.

amplitude and phase imbalance responses of the proposed hybrid coupler.

Obviously, the proposed coupler experiences a broadband impedance matching (S11 ≤ −21 dB) and strong isolation (S14 ≤ −21 dB) over the bandwidth of interest (27 GHz to 33 GHz). To examine the amplitude imbalance and phase imbalance over the operating frequency range, Fig. 4(b) is given. It can be found out that the proposed hybrid coupler covers the operating bandwidth with a phase tolerance of less than 1° and the amplitude imbalance of ± 0.5 dB.

III. WAVEGUIDE ANTENNA DESIGN

Technically, the conventional waveguide antenna has a simple structure in the form of the rectangular waveguide with wide impedance bandwidth as well as a broadside radiation pattern. However, this type of antenna typically suffers from the large aperture regarding the limited inter antenna element spacing (λ/2) in the uniform antenna array structures. Namely, WR28 with an aperture dimension of 7.112 mm × 3.556 mm with the cutoff frequency of 21.077 GHz is extensively used as a standard waveguide in the industry [28]. However, designing a waveguide antenna array at 30 GHz will be challenging because the aperture size (7.112 mm) is larger than the element spacing of 5 mm (corresponding λ/2), deterioration in the sidelobe level (SLL) [8].

In this paper, the SLLs are slightly sacrificed in lieu of design simplicity. Hence, to generate symmetrical radiation pattern in the azimuth plane maintaining design simplicity,

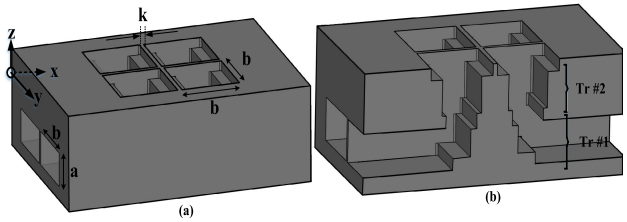

FIGURE 5. (a) 3-D view of the 2 × 2 open-ended waveguide antennas as radiating part of the proposed BSAN and (b) 3-D view of the 2 × 2 antennas when the side layer is partly removed. (a = 3.56 mm, b = 7.11 mm, k = 0.5 mm).

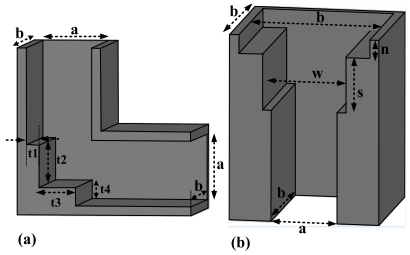

FIGURE 6. Two types of transitions; (a) Transition #1 for converting the horizontal WR28 to vertical WR28 and (b) Transition #2 for converting the WR28 (3.5 mm × 7.11 mm) to the antenna aperture size (7.11 mm × 7.11 mm). (a = 3.56 mm, b = 7.11 mm, t1 = 0.7 mm, t2 = 2.3 mm, t3 = 2mm, t4 = 1 mm, w = 4.5 mm, s = 3 mm, n = 1 mm).

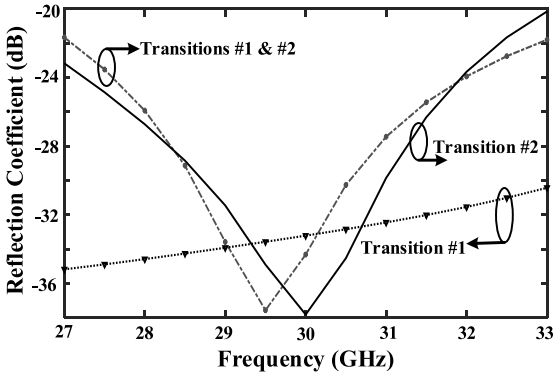

FIGURE 7. Frequency response of the reflection coefficient of the transitions shown in Figs. 5 (b) and 6.

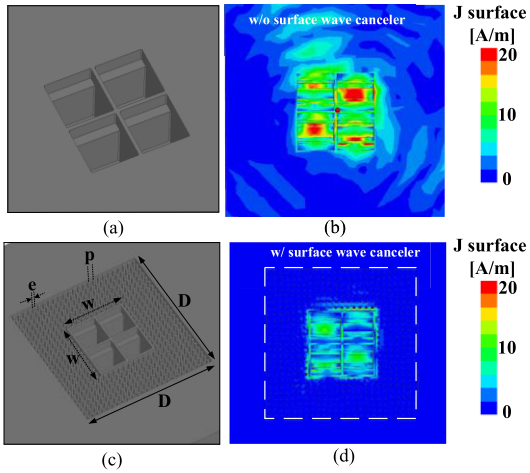

FIGURE 8. (a) Primary design of the 2 × 2 open-ended waveguide antenna aperture, (b) the simulation results of the induced surface current on the antenna aperture without employment of surface wave canceler, (c) the proposed design for antenna aperture surrounded by the metal pins as surface wave canceler (e = 0.6 mm, p = 1.43 mm, D = 30 mm, and w = 15.72 mm), and (d) the surface current distribution on the proposed design (with surface wave canceler).

the aperture size of the single waveguide antenna is designed in the form of a square. Fig. 5 depicts a sketch of the 2 × 2 open-ended waveguide antenna array. It can be observed that the antenna aperture is 7.1 mm × 7.1 mm, where it is fed by four WR28 input ports with dimensions 3.56mm × 7.11mm. To connect the WR28 feeding lines to the waveguide antenna, two types of transitions are essential, as shown in Fig. 5(b). For connecting the horizontal WR28 to vertical WR28, for converting WR28 (3.5 mm × 7.11 mm) to the antenna aperture size (7.11 mm × 7.11 mm). The 3-D view of the schematic of both the transitions along with the design parameters is exhibited in Fig. 6.

An optimization using Ansys HFSS [29] is performed to obtain a broadband transition over the bandwidth of interest. The frequency response of the reflection coefficient of two types of transitions are shown in Fig. 7. It is clear that both transitions have properly satisfied the impedance matching requirements (S11 ≤ -20 dB) over the bandwidth of interest (27 GHz – 33 GHz).

To realize the BSAN, all components including hybrid coupler, transitions, feeding network, and antenna elements are ready to be assembled in the entire design. However, the aperture 2 × 2 open-ended waveguide antenna due to the physical nature, which has been made of metal, suffers from the effects of induced surface waves, where they affect significantly the radiating performance of the proposed BSAN.

To address this problem, the authors proposed a set of the metal pins around the antenna aperture that behave as hard and soft surfaces. We are able to suppress and eliminate the induced surface waves around the aperture of the open-ended waveguide antennas, which it can be resulted in improving the SLL. In order to better realize this issue, Fig. 8 depicts the surface current induced on the antenna aperture in two different cases. In the first case as shown in Fig. 8 (a), the radiating part of the BSAN is without surface canceler.

As shown in Fig. 8(b), considerable current surface distribution is observed around the antenna aperture, which deteriorates the radiating performance of the proposed system with degrading SLLs. Alternatively, with employment the proposed solution as shown in Fig. 8 (c), the distribution of current surfaces has been suppressed significantly (see Fig. 8(d)), which it results in improving the total efficiency of the network. To realize how the proposed BSAN function, Fig. 9 is given.

The 3D radiation patterns of the proposed BSAN with respect to the exciting ports are individually observed (see Fig. 9). The total design of the proposed BSAN is shown in Fig. 10. As mentioned before the proposed network is

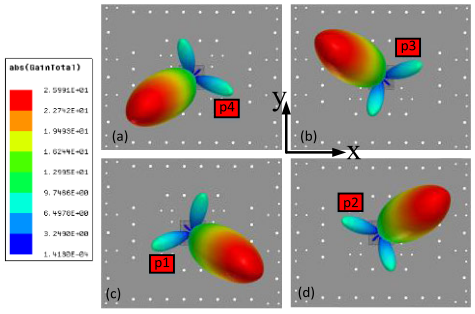

FIGURE 9. Simulated radiation patterns of the proposed BSAN at 30 GHz with respect to the exciting ports; (a) Port 4, (b) Port 3, (c) Port 1, and (d) Port 2.

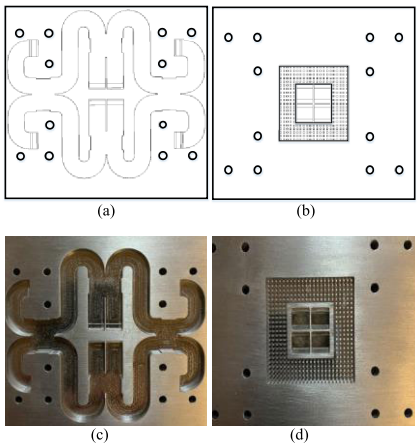

FIGURE 10. Proposed design of the BSAN; (a) a cut of the middle including the feeding network based on hollow waveguide, (b) the top view of the structure including the radiating part, (c) the feeding network in the first layer, and (d) photo of the second layer showing the 2 × 2 open-ended waveguide antenna.

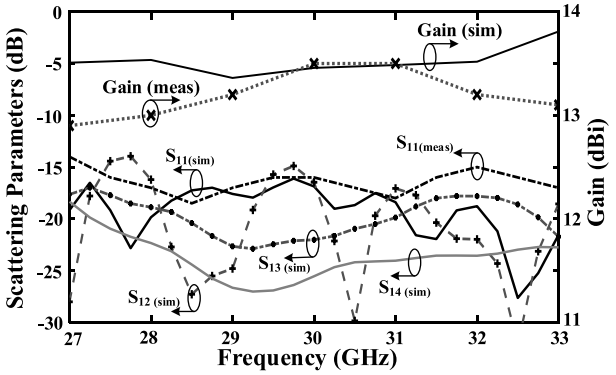

FIGURE 11. Measured and simulated results of the scattering parameters and gain of the proposed BSAN when it is excited by port 1.

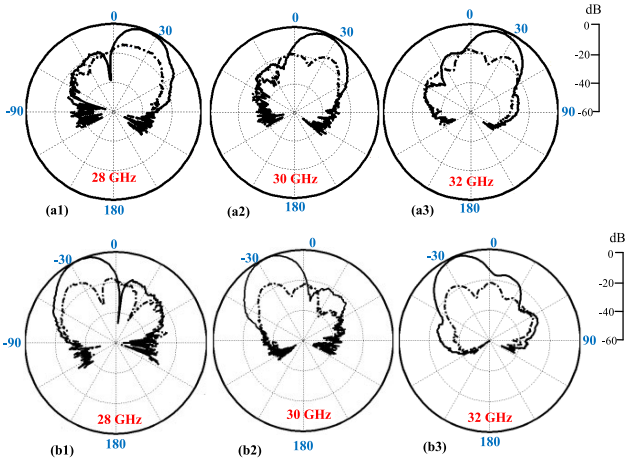

FIGURE 12. Measured radiation patterns of the proposed BSAN at frequencies of 28, 30, and 32 GHz when the BSAN is excited by (a) port 2 (up) and (b) port 1 (down). Note that solid and dashed lines represent the co- and cross-polarized results, respectively.

based on the hollow waveguide. To implement the design, the BSAN has to be cut from the middle, as exhibited in Fig. 10.

The feeding network of the BSAN including four hybrid couplers along with four input ports are apparently observed in Fig. 10 (a). From Fig. 10 (b) it can be observed that the radiating part of the network is comprised of 2 × 2 open-ended waveguide antennas, surrounded by the metal pins as the surface wave canceller. The photos of two layers of the fabricated BSAN are shown in Fig. 10 (c)–(d). The experimental and numerical results of the scattering parameters related to the proposed BSAN are presented in Fig. 11. It is notable that the results are obtained when one of the input ports is excited, namely port 1. Apparently, both the matching and isolation levels are at a strong level (≤ -15 dB) over the bandwidth of interest (27 GHz – 33 GHz). In addition, the gain curve of the proposed BSAN is shown in Fig. 11, as well. It can be observed that the simulated gain is higher than 13.5dBi over the bandwidth ($\theta = 20°$, $\varphi = 45°$).

It can be found out that the measured gain curve experiences a slight fluctuation of ±0.5 dBi over the frequency band of interest, demonstrating great agreement with the numerical results. It is notable that the gain and radiation pattern measurements were performed in an anechoic chamber system. The far-field measurement setup is tuned by moving the proposed BSAN along with the horn antenna only in the upper hemisphere (−120° to +120°) at an interval of 5° (due strictly to the measurement system restrictions). The experimental results of the radiation patterns, when the proposed BSAN is separately excited by ports 1 and 2, are depicted in Fig. 12. Obviously, the radiation patterns indicate an almost stable performance over the desired bandwidth.

IV. THE SIX-PORT NETWORK (SPN)

A. THEORITICAL DISCUSION

The six-port network (SPN) is a passive low cost circuit, which is composed of the hybrid couplers and/or power divider. The name ''six-port'' is directly derived from the structure itself.

It features two inputs, one for RF (unknown) signal and another one for the reference signal or local oscillation (LO),

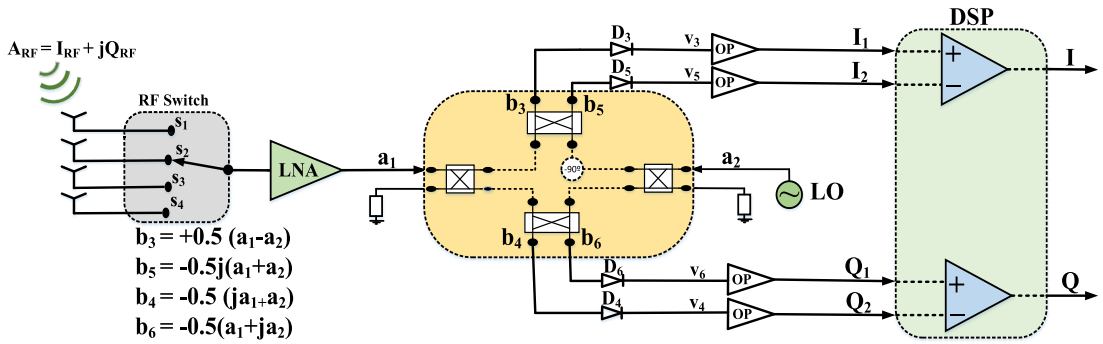

FIGURE 13. Block diagram of the analog front-end for down-conversion.

and four output ports, thus six ports [19]. The fundamental principle of the SPN can be expressed by phase-controlled superposition of two input signals RF and reference (LO) that are superimposed under four various relative and static phase shifts [30], [31]. One of the most efficient ways for the six-port's internal superposition of signals RF and LO is to select integer multiples of $\pi/2$ for the static phase shifts [31]. If the power of the input signals is identical, constructive, or destructive interaction occurs, depending on the values of the phase difference and amplitudes, respectively. After processing two signals in the radio-frequency (RF) domain, the results are down-converted to baseband [20].

As shown in Fig. 13, a block diagram of the analog front-end for down-conversion is presented. It can be seen that the RF signal is received by the BSAN, where it is controlled by RF switch (SP4T). Then, the received RF signal from the antenna is amplified by a low-noise amplifier (LNA), where supplies the received signal to port 1 as one of the input ports of the SPN. Note that the reference signal generated by the local oscillator (LO) feeds port 2 as another input ports of the SPN. In addition, two other ports of the SPN are terminated by two 50 Ω loads. According to Fig. 13, the scattering matrix of the SPN can be represented as follows;

$$[S] = \frac{1}{2}\begin{bmatrix} 0 & 0 & 1 & -j & -j & -1 \\ 0 & 0 & -1 & -1 & -j & -j \\ 1 & -1 & 0 & 0 & 0 & 0 \\ -j & -1 & 0 & 0 & 0 & 0 \\ -j & -j & 0 & 0 & 0 & 0 \\ -1 & -j & 0 & 0 & 0 & 0 \end{bmatrix} \tag{2}$$

The input signal for each port is denoted as a_i and the output signal for each port is indicated as b_i the waves. For the SPN (see Fig. 13), two complex input signals RF and reference can be expressed as [8]

$$a_1(t) = \alpha(t)\ a\, e^{j(\omega_0 t + \phi_1(t))} = \alpha(t)\ a_2\, e^{j(\omega_0 t + \Delta\phi(t))} \tag{3}$$

$$a_2 = a\, e^{j(\omega t + \phi_2)} \tag{4}$$

where two normalized incident signals experience an α amplitude ratio, $\Delta\varphi(t) = \varphi_1(t) - \varphi_2$ as phase difference, and $\Delta\omega(t) = \omega - \omega_0$ as frequency shift. Assuming a good match ($a_3 = a_4 = a_5 = a_6$), four normalized output waves can be indicated depending on the input waves and related scattering (s) parameters [19]

$$b_i = a_1 s_{1i} + a_2 s_{2i} \quad i = 3, \ldots, 6 \tag{5}$$

More particularly, here we have $b_3 = 1/2 \times (a_1 - a_2)$, $b_4 = -1/2 \times (ja_1 + a_2)$, $b_5 = -j/2 \times (a_1 + a_2)$, and $b_6 = -1/2 \times (a_1 + ja_2)$. To acquire the dc output signals, four power detectors should be connected to the SPN ports. It is noteworthy that the output dc voltage of an ideal power detector is proportional to the square magnitude of the RF input signal as follows [32]

$$v_i = \eta_i\ |b_i|^2 = \eta_i . b_i . b_i^*, \quad i = 3, \ldots, 6 \tag{6}$$

where the η_i constants are measured in v/w. The proposed SPN here operates as a direct demodulator. It means that $\omega = \omega_0$, corresponding to $\Delta\omega(t) = 0$. Assuming that four similar detectors are utilized, the dc output voltages are obtained, as [32]

$$v_3 = \eta\ |b_3|^2 = \eta\frac{a^2}{4}\left[1 + \alpha^2 - 2\alpha\cos(\Delta\varphi)\right] \tag{7}$$

$$v_4 = \eta\ |b_4|^2 = \eta\frac{a^2}{4}\left[1 + \alpha^2 - 2\alpha\sin(\Delta\varphi)\right] \tag{8}$$

$$v_5 = \eta\ |b_5|^2 = \eta\frac{a^2}{4}\left[1 + \alpha^2 + 2\alpha\cos(\Delta\varphi)\right] \tag{9}$$

$$v_6 = \eta\ |b_6|^2 = \eta\frac{a^2}{4}\left[1 + \alpha^2 + 2\alpha\sin(\Delta\varphi)\right] \tag{10}$$

In the complex plane, the χ vector can be defined using the four six-port dc output voltages [19], [32]

$$I = (v_5 - v_3) = \alpha\eta a^2\cos(\Delta\varphi) \tag{11}$$

$$Q = (v_6 - v_4) = \alpha\eta a^2\sin(\Delta\varphi) \tag{12}$$

Thus, this vector is denoted as [19], [32]

$$\chi = I + jQ = \alpha\eta a^2 e^{(j\Delta\varphi)} \tag{13}$$

Using (13), it can be found out that the magnitude of the χ vector is proportional to the ratio between the RF signal and the reference signal (LO), at ports 1 and 2, respectively.

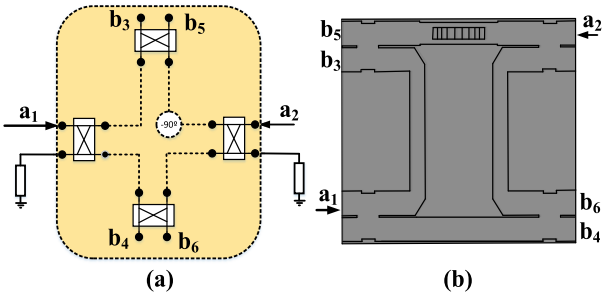

FIGURE 14. (a) The block diagram of the SPN including four 90° hybrid couplers and a 90° phase shifter and (b) the proposed design based on hollow waveguide showing all ports.

As a result, the vector indicates the analog direct demodulated signal [32], [33]. The baseband circuit is implemented with four two-stage conventional feedback operational amplifiers (AD8000) with a cut-off frequency of 800 MHz. The DC output voltages of the SPN are amplified by approximately 20 dB. Next, two differential amplifiers are needed to achieve I/Q signals with respect to (11) and (12). It should be noted that the desired bandwidth of the proposed BSAN and SPN here is 20% (27 GHz – 33 GHz). Thus, the bit rate is limited only by the speed of the baseband circuit. Correspondingly, with the use of the high-speed operational amplifiers, the speed of faster than a few hundreds Mb/s could be acquired.

B. THE SPN DESIGN

Using (13), it can be found out that the magnitude of the vector is proportional to the ratio between the RF signal at port 1 and the reference signal (LO) at port 2. As a result, the vector indicates the analog direct demodulated signal [19], [32]. As shown in Fig. 14, the architecture of the SPN, which is composed of four 90° hybrid couplers and 90° phase shifter, along with the proposed SPN implemented with hollow waveguide are demonstrated. Apparently, the input ports and other RF components (coupler and phase shifter) can be realized in waveguide point of view. In order to validate RF signal demodulation, the numerical results of scattering parameters of the SPN are shown in Fig. 15(a). Obviously, the RF and local signal ports of the SPN are well-matched in terms of impedance. In addition, the transmission between the RF input port and the four outputs is next to the theoretical value of −6 dB over a broad frequency band of interest.

One of the best analyses for validating the SPN performance is qi points [34]. This technique is particularly precious for broadband designs. The qi points include phase information and S-parameters from inputs of the SPN to outputs. These points are defined as:

$$q_i = -\frac{S_{2i}}{S_{1i}}, \quad i = 3, 4, 5, 6 \tag{14}$$

Using the equations (14) and (2), the qi points are −1, −j, 1, and j (ideal points). These points are ordered by 90° multiples and are placed equidistant from the origin of the complex plane. The phase difference between the pair of

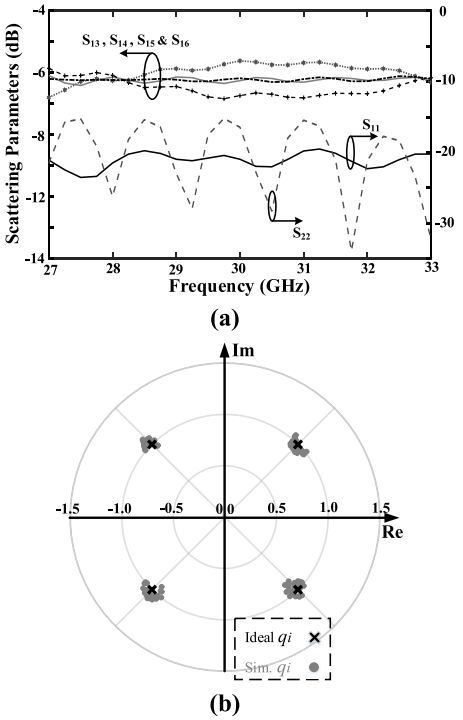

FIGURE 15. (a) Simulation results of the scattering parameters of the SPN, and (b) Polar plot of the ideal and simulated qi points.

odd (and also pair of even) qi points is 180°. Regarding the simulated S-parameters, the qi points of the proposed SPN are calculated and plotted in Fig. 15(b) over the bandwidth of interest (27 GHz – 33 GHz, and 250 MHz frequency resolution). A great achievement in terms of minimum errors of magnitude and phase is presented. It is observed that the bandwidth of the SPN is wide enough, and all points are very close to ideal positions.

It can be concluded that the proposed SPN receiver benefits from particular merits of low power, high speed, low loss, low noise, high efficiency, and broadband features, which all these properties give a promising value to the presented design for using in some applications such as low power wireless access point. One of the critical issues in communication systems is the system accuracy. To design frequency-independent phase shifter, the differential step-shaped phased shifter is suggested [35]. As exhibited in Fig. 16, the design parameters along with the values are given in the caption. The frequency response of the reflection coefficient and phase delay is indicated in Fig. 17. It can be observed that the impedance matching is strong ($|S11| \leq -20$ dB) over the frequency band of interest. Moreover, phase imbalance on 20% bandwidth (27 GHz – 33 GHz) is approximately 2°.

It is noteworthy that a 90° line delay might be employed instead of 90° phase shifter. However, for structures with broadband property one simple 90° line delay results in a considerable phase error on the desired bandwidth [36]. Realizing a 90° phase shifter using delay lines causes a high level of phase error, which could degrade the receiver efficiency

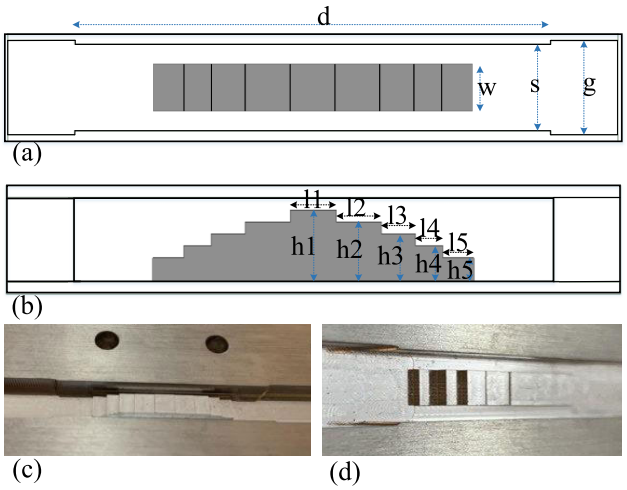

FIGURE 16. A 90° phase shifter with the design parameters (a) the top view and (b) side view. (w = 3.56, s = 6.5, g = 7.11, d = 35.9, l1 = 3.44, l2 = 3.37, l3 = 2.55, l4 = 2.06, l5 = 2.3, h1 = 2.21, h2 = 2.1, h3 = 2.03, h4 = 1.48, h5 = 0.6). Units in mm.

in terms of deteriorating sensitivity and pulse shape. For a delay line, the minimum phase error corresponds with the amount of phase delay × fractional bandwidth. Note that fractional bandwidth equals (f2–f1) / fc. Namely, phase delay and fractional bandwidth in this study are 90° and (33 GHz – 27 GHz) / 30GHz or 0.2, respectively. As a result, minimum phase error here corresponds to 18°, which simply states for a 90° delay line type with 20% impedance bandwidth a 18° phase imbalance will be inevitable. The whole idea rests on the fact that a delay line as phase shifter will be a frequency-dependent component. As known, an SPN can be designed using four hybrid couplers and one 90° phase shifter. To satisfy the SPN accuracy conditions, a precise 90° phase difference between the outputs in the individual coupler has to be obtained. However, in practice, the phase difference is not precisely 90° because of process variations. As shown in Fig. 18, there exist different phase errors in a typical SPN, two of them belong to the hybrid couplers connected to each other and one is associated with a phase shifter. Yang in [23] has expressed other errors including the dynamic dc offset voltage in addition to the mismatches of the diode characteristics in the power detector. Authors in this study mostly focus on the phase issues in the SPN to improve bit error ratio (BER). With respect to the phase errors discussed above and indicated in Fig. 16, the output signals in each port can be expressed as

$$b_3 = \frac{1}{2}\left\{a_1 + a_2\left[e^{j(-\frac{\pi}{2}+\psi)} \times e^{j(-\frac{\pi}{2}+\xi)}\right]\right\} \quad (15)$$

$$b_4 = \frac{1}{2}\left\{a_1\left[e^{j(-\frac{\pi}{2}+\xi)}\right] + a_2\left[e^{j(-\pi+2\xi)}\right]\right\} \quad (16)$$

$$b_5 = \frac{1}{2}\left\{a_1\left[e^{j(-\frac{\pi}{2}+\xi)}\right] + a_2\left[e^{j(-\frac{\pi}{2}+\psi)}\right]\right\} \quad (17)$$

$$b_6 = \frac{1}{2}\left\{a_1\left[e^{j(-\pi+2\xi)}\right] + a_2\left[e^{j(-\frac{\pi}{2}+\xi)}\right]\right\} \quad (18)$$

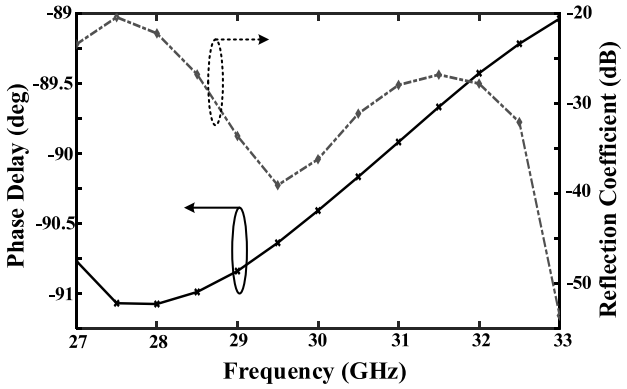

FIGURE 17. Simulation results of the proposed phase shifter.

As mentioned before, the output voltage of an ideal power detector is proportional to the square magnitude of the RF input signal using (6), the DC output voltages are achieved, respectively, as

$$v_3 = k\ |b_3|^2 = \frac{k}{4}\left\{\begin{array}{l} a_1^2 + a_2^2 e^{2j(-\pi+\xi+\psi)} \\ +2a_1a_2e^{j(-\pi+\xi+\psi)} \end{array}\right\} \quad (19)$$

$$v_4 = k\ |b_4|^2 = \frac{k}{4}\left\{\begin{array}{l} a_1^2 e^{2j(-\frac{\pi}{2}+\xi)} \\ +a_2^2 e^{2j(-\pi+2\xi)} \\ +2a_1a_2e^{j(-\frac{3\pi}{2}+3\xi)} \end{array}\right\} \quad (20)$$

$$v_5 = k\ |b_5|^2 = \frac{k}{4}\left\{\begin{array}{l} a_1^2 e^{2j(-\frac{\pi}{2}+\xi)} \\ +a_2^2 e^{2j(-\frac{\pi}{2}+\psi)} \\ +2a_1a_2e^{j(-\pi+\xi+\psi)} \end{array}\right\} \quad (21)$$

$$v_6 = k\ |b_6|^2 = \frac{k}{4}\left\{\begin{array}{l} a_1^2 e^{2j(-\pi+2\xi)} \\ +a_2^2 e^{2j(-\frac{\pi}{2}+\xi)} \\ +2a_1a_2e^{j(-\frac{3\pi}{2}+3\xi)} \end{array}\right\} \quad (22)$$

Thus, considering the phase errors in the proposed equations (19) to (22), the high level of calibration with excellent accuracy could be carried out. To further understand, Figs. 19 and 20 are given, where time behaviour of the demodulated QPSK signals with the phase variations are shown. As illustrated in Fig. 19, the simulation signals of QPSK with phase error variation of phased shifter (ψ) for inputs and outputs of I and Q are represented. It can be found out that the output I is varying with phase variation of phase shifter while output Q remains without change.

Fig. 20 gives the simulation signals of QPSK with phase error variation of hybrid couplers (ξ) for inputs and outputs of I and Q. It can be realized that both outputs of I and Q are slightly affected by phase error variation of couplers (ξ). To clearly realize, the constellation of the demodulated QPSK signals with the phase error variations in phase shifter (ψ) and hybrid couplers (ξ) is shown in Fig. 21. As expected from (19) to (22), it can be observed that the phase error in phase shifter (ψ) affects only the real part (output I) while the phase error in hybrid couplers (ξ) affects both the real and imaginary parts (output I and Q). The photo of the fabricated design is shown in Fig. 22. It can be observed that the proposed design consists

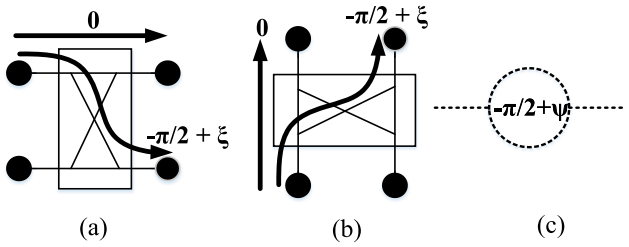

FIGURE 18. Phase errors in the SPN including four 90° hybrid couplers and one 90° phase shifter; (a) phase errors in horizontal couplers terminated to the input ports, (b) phase errors in vertical couplers terminated to output ports, and (c) phase error in a 90° phase shifter (see the SPN topology in Fig. 14). Note that due to the identical hybrid couplers, the phase error in two couplers are the same (ξ).

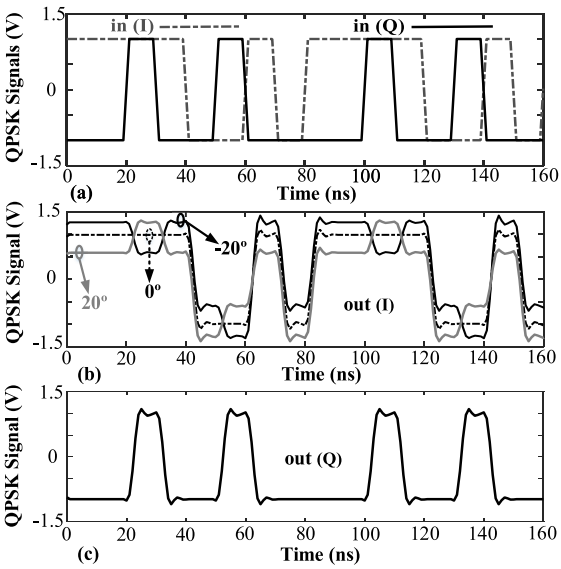

FIGURE 19. Simulated signals of QPSK versus the time, (a) input I and Q, (b) output I, and (c) output Q. Note that output I is changing with phase variation of phase shifter while output Q remains without change.

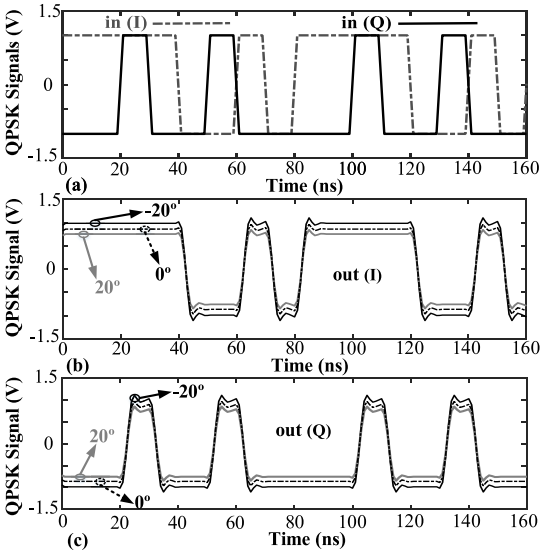

FIGURE 20. Simulated signals of QPSK versus the time, (a) input I and Q, (b) output I, and (c) output Q. Note that both outputs of I and Q are changing with phase variation of hybrid couplers.

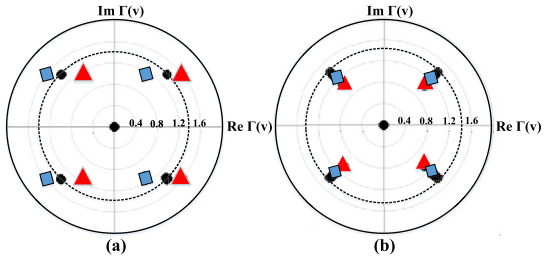

FIGURE 21. Constellation of the demodulated QPSK signals with considering the phase error variation of (a) phase shifter and (b) hybrid coupler. (a) when phase in a phase shifter is changed from −20°, 0°, and 20°, results are indicated in the form of the triangle, circle, and square respectively. (b) when phase error (ξ) in hybrid coupler is varied from 0°, 20°, and 40°, results are indicated in the form of circle, square, and triangle respectively.

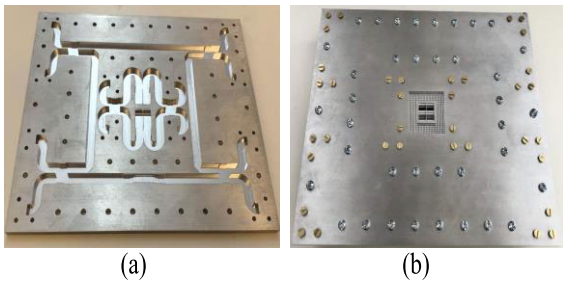

FIGURE 22. Fabrication photo of the two-layer proposed design (a) the bottom layer including the waveguide feeding network for the BSAN and SPN and (b) the top layer including the radiating antenna elements.

of two layers. The bottom layer is composed of the waveguide feeding network for the BSAN and SPN (see Fig. 22(a)). The top layer is comprised of the radiating antenna elements, as shown in Fig. 22(b).

Besides, system simulations here are performed using advanced design system (ADS) software of Keysight Technologies with a system module. Using ADS software, the transmitter employs a vector modulator (VM) to achieve the PSK and QAM modulated signal. Diverse modulations (QPSK, 16 PSK, 16 QAM, and 32 QAM) are generated and determined.

Note that the operating frequency of 30GHz is adjusted while doing the simulations by the envelope simulation in ADS. Fig. 23 depicts the simulated constellation of the demodulated signal achieved for different modulation schemes. It can be realized that the proposed system behaves as an acceptable analog demodulator. In the case of PSK modulations, the constellation points form a circle, with respect to equation (13). Moreover, for the case of the 16 QAM modulations, the points are approximately equidistant, satisfying the front-end discrimination's qualities in both amplitude and phase. In the PSK modulations, the constellation points are almost observed in a circle. Moreover, in the 16 QAM modulations, the points are approximately equal distances, indicating the quality of the front-end discrimination for both amplitude and phase are nearly satisfactory. Ideally, because of the SPN design and the differential approach utilized in the

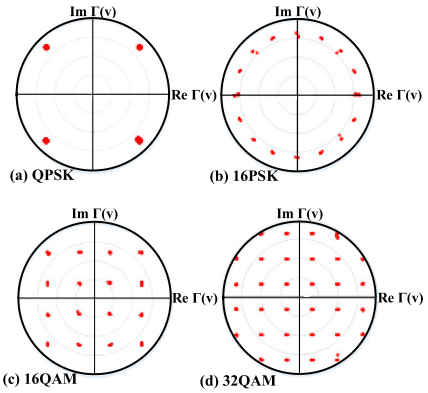

FIGURE 23. Simulated constellation of the demodulated PSK/QAM signals without noise.

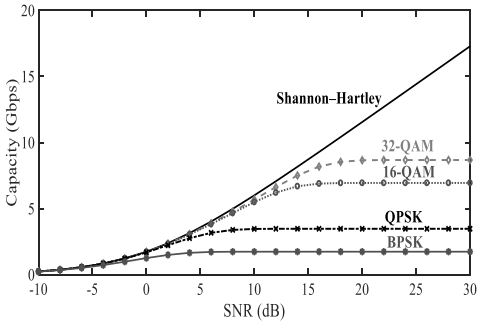

FIGURE 24. Channel capacity for the proposed developed system associated with the BPSK, QPSK, 16QAM, and 32QAM modulations.

baseband section, the phase error at the operating frequency is negligible. As a result, the constellation of any PSK signal is obtained with high accuracy. Note that the errors produced in amplitude have taken root in the nonlinearity of the power detectors. In addition, the phase of the reference signal (LO) has to be tuned to avoid the constellation rotation.

V. SYSTEM RESULTS

A. CHANNEL CAPACITY

While investigating a radio link performance, it worth understanding the achievable maximum data rate that can be transmitted through the channel. The RF engineers utilize the concept of Shannon–Hartley channel capacity to determine the maximum data rate, and it is given as following:

$$C = B\ \log_2(1+\gamma) \tag{23}$$

where B is the operating frequency bandwidth, and γ is the signal to noise ratio. The achievable channel capacity for the proposed developed system associated with the BPSK, QPSK, 16QAM, and 32QAM modulations are given in Fig. 24.

B. BEAMFORMER INFLUENCE ON CHANNEL PERFORMANCE IMPROVEMENT

The received signal by the receiver antenna beamformer can be evaluated using Friis equation as following:

$$P_r(dBm) = P_t(dBm) + G_t(dBi) + G_r(dBi) - PL(dBm) \tag{24}$$

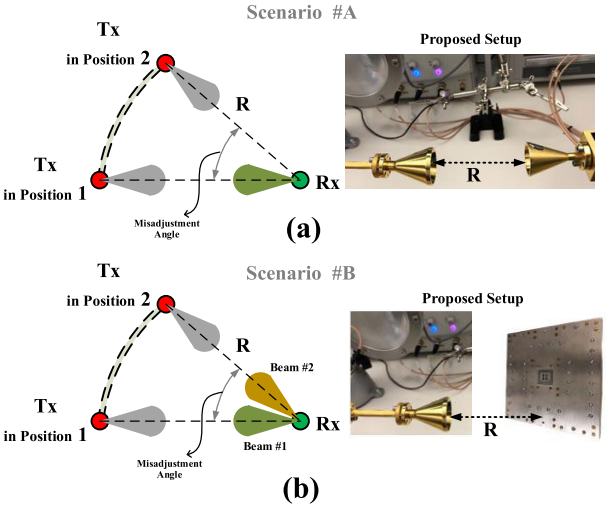

FIGURE 25. Defined scenarios to investigate the beamformer capability for improving link performance. (a) The proposed system with directive horn antenna with 8° beam width. (b) The proposed system with the proposed beamformer. Scenario #B is given for the rotated xz–plane, where beam #1 and beam #2 are radiated.

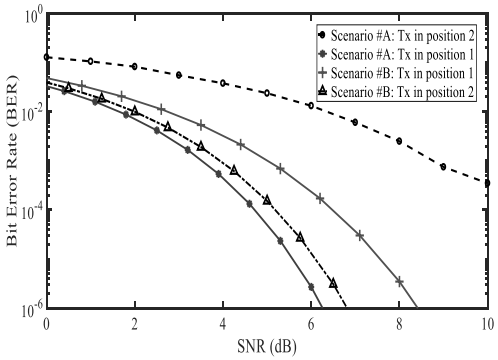

FIGURE 26. Simulation BER performance for QPSK modulation with 6 GHz bandwidth and data rate of 1 Gb/s, concerning the defined scenarios in Fig. 25.

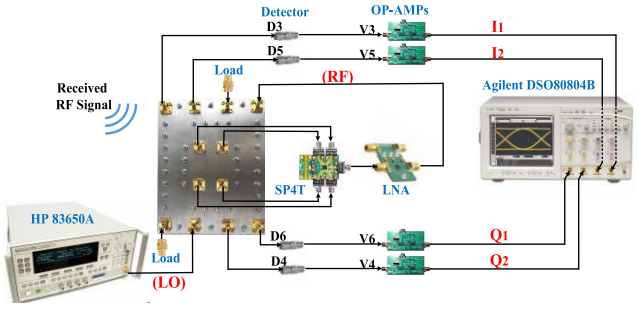

FIGURE 27. Full test setup for the proposed broadband zero-IF receiver.

where Pr and Pt are the received and transmitted powers, Gt and Gr are the transmitter and receiver antennas' gains, respectively. PL is the propagation channel path loss, and is given as follow:

$$PL(dBm) = -20\ \log\left(\frac{\lambda}{4\pi R}\right) \tag{25}$$

where R is the distance between the transmitter and receiver, and λ is the wavelength at free-space wavelength. For

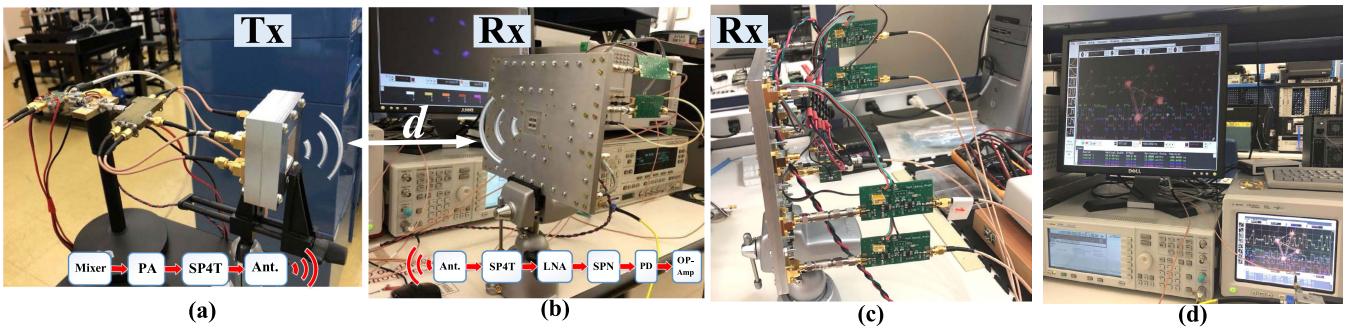

FIGURE 28. Digital photograph of the experimental test bench, (a) transmitter setup, (b) receiver setup, (c) side view of the fabricated design, and (d) demodulated signals on the oscilloscope. (d: distance between transmitter and receiver antennas, PA: power amplifier, SPN: six port network, and PD: power detector).

instance, for a 30-GHz radio signal, the propagation channel path loss is about 61.98 dB over a one-meter distance. It is notable that in the Friis equation, the atmospheric losses and contribution to multipath reflected waves in the received power are not considerable. However, in an office environment, it is observed that a communication link with narrow radiation beams follows the Friis model closely. The results for a system with directive horn antenna (radiation pattern beamwidth) at 30-GHz confirm that a small beams' misadjustment deteriorates the link budget about 10 dB. As a result, the highest throughput would degrade QPSK modulation signals with a bandwidth of 6 GHz by up to 3 Gbps or disconnect the communication link entirely. Fig. 25 shows defined scenarios for evaluating the beamformer capability to improve link performance. The simulated BER performance of the defined scenarios in Fig. 26 is investigated to evaluate the potential of the proposed beamformer for QPSK modulation with a bandwidth of 6 GHz and a data rate of 1 Gb/s. The architecture of the analog front-end for 30 GHz down-conversion (zero-IF) system is configured and implemented utilizing available equipment, as illustrated in Fig. 27.

The setup hence is composed of the proposed design including 2 × 2 BSAN along with the SPN in one package, the SP4T switch, low-noise amplifier (LNA), industrial planar power detectors (603AK, Krytar), and current feedback operational amplifiers type AD8000. In short, the zero-IF receiver operates as follows, through the BSAN and SP4T RF switch, the received RF signal goes to an LNA (HMC-1040LP3CE) to amplify (27–33 GHz, 23 dB gain, NF = 2.2 dB). The reference signal from the local oscillator (LO) enters the intended port (port 2) in the proposed SPN. Note that for all twelve input and output ports, WR28 waveguide to coaxial adapters K (2.92mm) are used. To obtain the baseband signal, four outputs of the SPN are connected to four RF power detectors. In addition, the received signal is at a weak level. So to do, amplifying output voltage signals for better detection and BER measurements sounds reasonable. As a result, amplifiers type AD8000 are used to tackle this shortcoming. Ultimately, the Ka-band SPN receiver is measured with respect to bench setup shown in Fig. 27. On the other hand, the transmitted signal is a modulated signal, which

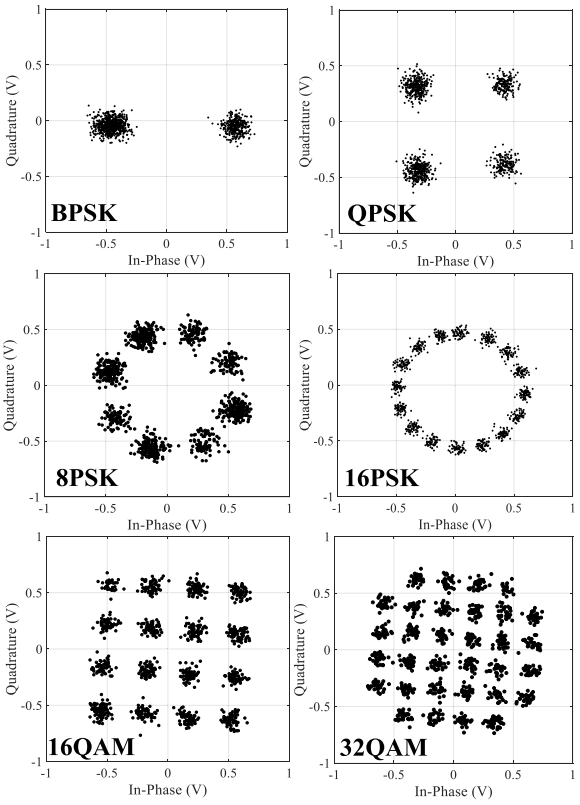

FIGURE 29. Measurement constellation results of the demodulated PSK/QAM signals for different symbols.

is up-converted from IF to Ka-band utilizing an industrial sub-harmonic mixer evaluation kit (EVAL-HMC338LC3B). Then this signal is amplified by a medium power amplifier (HMC281LM1), entered an SP4T RF switch, and transmitted by the 2×2 antenna beamformer based on an air-filled coaxial line designed by the same authors [8].

System parameters are: the transmitting antenna has a gain of 16 dBi, the distance between transmitter and receiver (d) is 3 m, and the transmitted power is around +10 dBm. The four output signals (I1, I2, Q1, Q2) from the 30 GHz front-end SPN receiver, are displayed and recorded using an Agilent Infiniium high-performance oscilloscope (DSO80804B). The

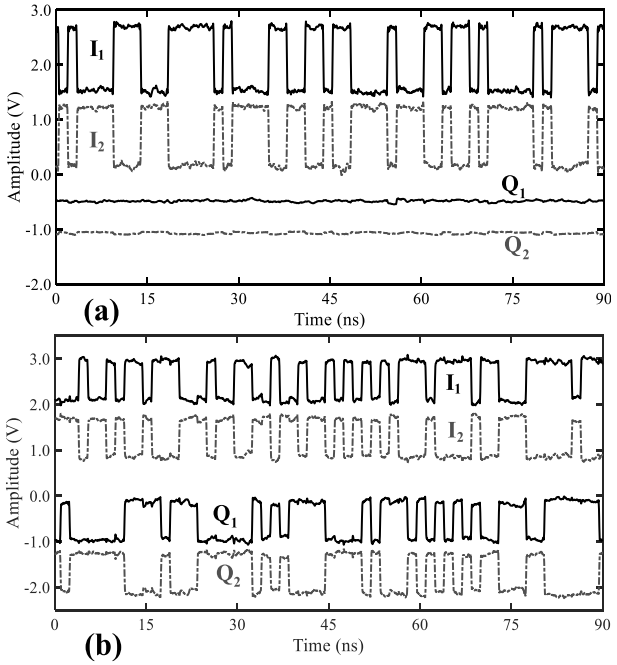

FIGURE 30. Measured demodulation signals of I and Q versus time. (a) BPSK, and (b) QPSK.

photo of the entire measurement setup for the proposed transceiver is exhibited in Fig. 28.

The demodulation results of PSK/QAM signals, from 2 to 32 symbols, are thus captured as illustrated in Fig. 29. It can be realized that the symbols of BPSK, 8PSK, and 16PSK demodulations almost form a circle. In the same manner, for the QPSK constellation diagram, a quasi-perfectly square shape is obtained. For the cases of the 16QAM and 32QAM, the points are nearly equidistant, fulfilling the front-end discrimination's qualities in both amplitude and phase, with respect to the SPN demodulation theory [37], [38].

As a note, the errors are based on mostly because of the synchronization of transmitting and receiving equipment (phase noise), along with the fabrication inaccuracy (symmetry of the constellation points) [37], [38]. Fig. 30 shows the measured pseudorandom sequence of the demodulated I1, I2, Q1, and Q2 output voltage signals over the time for the receiver at the operating frequency of 29 GHz. As observed in the Figure, if we consider the level of demodulated BPSK signal as a peak value, both demodulated signals of QPSK have the same amplitude and equal to 0.707 of the peak. The waveforms are approximately rectangular, due to the uses of high-speed baseband circuits. Moreover, phase jumps of the signals of the I and Q correspond with multiples of 90°. Also, the output pair voltages (I1 and I2, and Q1 and Q2, respectively) are phase opposite. Therefore, the main I/Q signals can be achieved by applying a differential method, as discussed before in (11) and (12). It can be found out that errors of the phase and amplitude are minor, not exceeding a few per cents for individual constellation points.

VI. CONCLUSION

A zero-IF receiver with broadband and high-efficiency properties based on hollow waveguide technology for the wireless access point (WAP) applications is introduced. The principal advantage of the waveguide technologies is that they support propagation with lower losses at mmWave bands. The focus of this project is to present an integrated beam-switching antenna network (BSAN) with a six-port network (SPN) homodyne receiver in waveguide technology to eliminate possible transitions in the first stages, and decrease the insertion losses and noise levels. The receiver is composed of a Ka-band BSAN with a two-dimensional (2D) scanning feature. For demodulation, the receiver is designed utilizing a highly efficient broadband SPN. The proposed SPN is comprised of four 90° hybrid couplers and a 90° phase shifter. For broadband receivers, it was observed that delay line type of phased shifter deteriorates considerably the performance and efficiency of the system. Therefore, to reduce the phase imbalance over the frequency band, a step-shaped phase shifter having a frequency-independent property with the minimum phase error is designed. Moreover, a theoretical and experimental analysis of the SPN phase errors under different modulations was carried out and represented. Channel capacity along with beamformer effect on channel performance improvement are represented and analyzed. Experimental results indicate excellent agreement with the simulations. Ultimately, the proposed zero-IF receiver presents a promising option for low-power wireless access point communications, robust military applications, or as a front-end at extremely low temperatures to decrease noise levels.

REFERENCES

[1] M. Akbari, A. Farahbakhsh, and A.-R. Sebak, "Ridge gap waveguide multilevel sequential feeding network for high-gain circularly polarized array antenna," *IEEE Trans. Antennas Propag.*, vol. 67, no. 1, pp. 251–259, Jan. 2019.

[2] M. Akbari, M. Farahani, A. Ghayekhloo, S. Zarbakhsh, A.-R. Sebak, and T. A. Denidni, "Beam tilting approaches based on phase gradient surface for mmWave antennas," *IEEE Trans. Antennas Propag.*, vol. 68, no. 6, pp. 4372–4385, Jun. 2020.

[3] M. Akbari, S. Gupta, M. Farahani, A. R. Sebak, and T. A. Denidni, "Gain enhancement of circularly polarized dielectric resonator antenna based on FSS superstrate for MMW applications," *IEEE Trans. Antennas Propag.*, vol. 64, no. 12, pp. 5542–5546, Dec. 2016.

[4] S. Zarbakhsh, M. Akbari, F. Samadi, and A.-R. Sebak, "Broadband and high-gain circularly-polarized antenna with low RCS," *IEEE Trans. Antennas Propag.*, vol. 67, no. 1, pp. 16–23, Jan. 2019.

[5] M. Akbari, H. A. Ghalyon, M. Farahani, A.-R. Sebak, and T. A. Denidni, "Spatially decoupling of CP antennas based on FSS for 30-GHz MIMO systems," *IEEE Access*, vol. 5, pp. 6527–6537, 2017.

[6] *FCC and LMDS*. Accessed: Apr. 1, 2020. [Online]. Available: https://transition.fcc.gov/Bureaus/Wireless/Factsheets/lmds.html

[7] *Wireless Access Point (WAP)*. Accessed: Jun. 1, 2021. [Online]. Available: https://www.linksys.com/us/r/what-is-a-wifi-range-extender/what-is-a-wifi-access-point/

[8] M. Akbari, M. Farahani, S. Zarbakhsh, M. D. Ardakani, A.-R. Sebak, T. A. Denidni, and O. M. Ramahi, "Highly efficient 30 GHz 2×2 beamformer based on rectangular air-filled coaxial line," *IEEE Trans. Antennas Propag.*, vol. 68, no. 7, pp. 5236–5246, Jul. 2020.

[9] P. Chen, W. Hong, Z. Kuai, and J. Xu, "A double layer substrate integrated waveguide Blass matrix for beamforming applications," *IEEE Microw. Wireless Compon. Lett.*, vol. 19, no. 6, pp. 374–376, Jun. 2009.

[10] Y. Gao, M. Khaliel, F. Zheng, and T. Kaiser, "Rotman lens based hybrid analog–digital beamforming in massive MIMO systems: Array architectures, beam selection algorithms and experiments," *IEEE Trans. Veh. Technol.*, vol. 66, no. 10, pp. 9134–9148, Oct. 2017.
[11] T. Djerafi, N. J. G. Fonseca, and K. Wu, "Broadband substrate integrated waveguide 4 × 4 Nolen matrix based on coupler delay compensation," *IEEE Trans. Microw. Theory Techn.*, vol. 59, no. 7, pp. 1740–1745, Jul. 2011.
[12] M. M. M. Ali and A.-R. Sebak, "2-D scanning magnetoelectric dipole antenna array fed by RGW butler matrix," *IEEE Trans. Antennas Propag.*, vol. 66, no. 11, pp. 6313–6321, Nov. 2018.
[13] T. Djerafi and K. Wu, "A low-cost wideband 77-GHz planar butler matrix in SIW technology," *IEEE Trans. Antennas Propag.*, vol. 60, no. 10, pp. 4949–4954, Oct. 2012.
[14] S. O. Tatu, E. Moldovan, K. Wu, and R. G. Bosisio, "A new direct millimeter-wave six-port receiver," *IEEE Trans. Microw. Theory Techn.*, vol. 49, no. 12, pp. 2517–2522, Dec. 2001.
[15] J. Li, R. G. Bosisio, and K. Wu, "Computer and measurement simulation of a new digital receiver operating directly at millimeter-wave frequencies," *IEEE Trans. Microw. Theory Techn.*, vol. 43, no. 12, pp. 2766–2772, Dec. 1995.
[16] S. O. Tatu, E. Moldovan, and S. Affes, "Multi-port front-end and transceivers for V-band multi-gigabit/s communication systems," in *Digital Front-End in Wireless Communications and Broadcasting: Circuits and Signal Processing*, F.-L. Luo, Ed. Cambridge, U.K.: Cambridge Univ. Press, Sep. 2011, pp. 707–732.
[17] S. B. Chon and N. P. Weinhouse, "An automatic microwave phase measurement system," *Microw. J.*, vol. 7, no. 2, pp. 49–56, 1964.
[18] G. F. Engen and C. A. Hoer, "Application of an arbitrary 6-port junction to power-measurement problems," *IEEE Trans. Instrum. Meas.*, vol. IM-21, no. 4, pp. 470–474, Nov. 1972.
[19] G. F. Engen, "The six-port reflectometer: An alternative network analyzer," *IEEE Trans. Microw. Theory Techn.*, vol. MTT-25, no. 12, pp. 1075–1080, Dec. 1977.
[20] A. Koelpin, G. Vinci, B. Laemmle, D. Kissinger, and R. Weigel, "The sixport in modern society," *IEEE Microw. Mag.*, vol. 11, no. 7, pp. 35–43, Nov./Dec. 2010.
[21] J. Li, R. G. Bosisio, and K. Wu, "A six-port direct digital millimeter wave receiver," in *IEEE MTT-S Int. Microw. Symp. Dig.*, May 1994, pp. 79–82.
[22] G. F. Engen, "Calibrating the six-port reflectometer by means of sliding terminations," *IEEE Trans. Microw. Theory Techn.*, vol. MTT-26, no. 12, pp. 951–957, Dec. 1978.
[23] J.-R. Yang, D.-W. Kim, and S. Hong, "A calibration method of a range finder with a six-port network," *IEEE Microw. Wireless Compon. Lett.*, vol. 17, no. 7, pp. 549–551, Jul. 2007.
[24] P. Baniya and K. L. Melde, "Switched-beam endfire planar array with integrated 2-D butler matrix for 60 GHz chip-to-chip space-surface wave communications," *IEEE Antennas Wireless Propag. Lett.*, vol. 18, no. 2, pp. 236–240, Feb. 2019.
[25] M. Farahani, M. Akbari, M. Nedil, T. A. Denidni, and A. R. Sebak, "A novel low-loss millimeter-wave 3-dB 90° ridge-gap coupler using large aperture progressive phase compensation," *IEEE Access*, vol. 5, pp. 9610–9618, 2017.
[26] M. Farahani, M. Akbari, M. Nedil, A.-R. Sebak, and T. A. Denidni, "Millimeter-wave dual left/right-hand circularly polarized beamforming network," *IEEE Trans. Antennas Propag.*, vol. 68, no. 8, pp. 6118–6127, Aug. 2020.
[27] S. Yamamoto, J. Hirokawa, and M. Ando, "Length reduction of a short slot directional coupler in a single-layer dielectric substrate waveguide by removing dielectric near the side walls of the coupler," *IEEE Antennas Propag. Soc. Symp.*, vol. 3, Jun. 2004, pp. 2353–2356.
[28] *Rectangular Waveguide Sizes*. Accessed: Apr. 1, 2020. [Online]. Available: https://www.everythingrf.com/techresources/waveguides-sizes
[29] (2018). *ANSYS HFSS*. ANSYS, Inc. Accessed: Apr. 1, 2020. [Online]. Available: www.ansys.com/products/electronics/ansys-hfss
[30] G. Vinci, S. Lindner, F. Barbon, S. Mann, M. Hofmann, A. Duda, R. Weigel, and A. Koelpin, "Six-port radar sensor for remote respiration rate and heartbeat vital-sign monitoring," *IEEE Trans. Microw. Theory Techn.*, vol. 61, no. 5, pp. 2093–2100, May 2013.
[31] A. Koelpin, F. Lurz, S. Linz, S. Mann, C. Will, and S. Lindner, "Six-port based interferometry for precise radar and sensing applications," *Sensors*, vol. 16, no. 10, p. 1556, Sep. 2016.
[32] S. O. Tatu, E. Moldovan, K. Wu, R. G. Bosisio, and T. A. Denidni, "Ka-band analog front-end for software-defined direct conversion receiver," *IEEE Trans. Microw. Theory Techn.*, vol. 53, no. 9, pp. 2768–2776, Sep. 2005.
[33] S. O. Tatu, A. Serban, M. Helaoui, and A. Koelpin, "Multiport technology: The new rise of an old concept," *IEEE Microw. Mag.*, vol. 15, no. 7, pp. S34–S44, Nov. 2014.
[34] S. O. Tatu and K. Wu, "Six-port technology and applications," in *Proc. 11th Int. Conf. Telecommun. Modern Satell., Cable Broadcast. Services (TELSIKS)*, Oct. 2013, pp. 239–248.
[35] J. L. Cano, A. Mediavilla, and A. Tribak, "Parametric design of a class of full-band waveguide differential phase shifters," *Electronics*, vol. 8, no. 3, p. 346, Mar. 2019.
[36] M. Farahani, M. Nedil, and T. A. Denidni, "A novel hedgehog waveguide and its application in designing a phase shifter compatible with hollow waveguide technology," *IEEE Trans. Microw. Theory Techn.*, vol. 67, no. 10, pp. 4107–4117, Oct. 2019.
[37] C. Hannachi and S. O. Tatu, "Millimeter-wave multi-port front-end receivers: Design considerations and implementation," *Advanced Electronic Circuits-Principles, Architectures and Applications on Emerging Technologies*. Rijeka, Croatia: In-Tech Publications, 2018, ch. 4, pp. 85–103.
[38] M. D. Ardakani, C. Hannachi, B. Zouggari, E. Moldovan, and S. O. Tatu, "Accurate millimeter-wave carrier frequency offset measurement using the six-port interferometric technique," in *Proc. 48th Eur. Microw. Conf. (EuMC)*, Sep. 2018, pp. 1061–1064.

MOHAMMAD AKBARI (Member, IEEE) received the Ph.D. degree in electrical and computer engineering from Concordia University, Montreal, QC, Canada, in 2018. He was a Postdoctoral Fellow with the University of Waterloo, Waterloo, ON, Canada. Since July 2020, he has been a member of the Electromagnetic Vision (EMVi) Research Laboratory, McMaster University, Hamilton, ON, Canada. He is the author or coauthor of more than 80 peer-reviewed scientific journal articles and international conference papers. His current research interests include reconfigurable antenna, phased array antenna, metasurface and metamaterials, miniaturization approaches, mutual coupling reduction techniques, feeding networks, RCS reduction, polarizer, and ultra-wideband (UWB) technology. He was a recipient of the Postdoctoral Fellowships from the Fonds de recherche du Québec – Nature et technologies (FRQNT), in 2019, the PERSWADE/NSERC-Create Training Program Award, in 2017, the Accelerator Award, in 2017, the Graduate Concordia Merit Scholarship, in 2016, and the Concordia University International Tuition Fee Remission, in 2014. He served as a Reviewer for the IEEE Antennas and Propagation Society's journals and magazine.

MOHAMMADMAHDI FARAHANI (Member, IEEE) received the M.Sc. degree in electrical engineering, applied electromagnetics from the Iran University of Science and Technology (IUST), Tehran, Iran, in 2012, and the Ph.D. degree in telecommunications engineering from the Institut National de la Recherche Scientifique (INRS-EMT), Université du Québec, Montreal, QC, Canada, in 2020. He was a Researcher at the IUST Antennas and Microwave Research Laboratory, RF Communication's Systems Group, from 2009 to 2012. He is currently a Postdoctoral Researcher with the Department of Electrical and Computer Engineering, Concordia University. He is the author or coauthor of more than 30 peer-reviewed scientific journal articles and international conference papers and holds one patent. His current research interests include phased array antennas, switched multi-beam antenna arrays, FSS structures, dielectric resonator antennas, metamaterial antennas, and microwave components development for wireless communications systems. He was a recipient of the Postdoctoral Fellowships from Fonds de recherche du Québec – Nature et technologies (FRQNT), and Concordia University Horizon, in 2020.

MANSOOR DASHTI ARDAKANI received the B.Sc. degree in electrical engineering from the Shiraz University of Technology, Iran, in 2009, and the M.Sc. degree in electrical and telecommunications engineering from the Iran University of Science and Technology (IUST), Tehran, Iran, in 2012. He is currently pursuing the Ph.D. degree with the Institut National de la Recherche Scientifique (INRS-EMT), Université du Québec, Montreal, QC, Canada. He worked with Teyf Ertebat Ltd., Tehran, as an RF Engineer and the Project Manager, from 2011 to 2014, and as the Technical Manager, from 2014 to 2016. His current research interests include the microwave and millimeter-wave circuits, wireless systems and transceivers, radars, RF modules, antennas, and microwave measurement techniques. He was a recipient of the Fonds de Recherche du Québec–Nature et Technologies (FRQNT) Doctoral and Postdoctoral Fellowships, in 2018 and 2021, respectively.

ALI LALBAKHSH (Member, IEEE) received the B.S. and M.S. degrees in electronic and telecommunication engineering, in 2008 and 2011, respectively, and the Master of Research (M.Res.) and Ph.D. degrees in electronics engineering from Macquarie University, Australia, in 2015 and 2020, respectively. He currently holds an academic position (Macquarie University Research Fellowship) at Macquarie University. He has published over 80 peer-reviewed journal articles and conference papers. His research interests include satellite communication, high-gain antennas, evolutionary optimization methods, and passive microwave components. He received several prestigious awards, including the International Research Training Program Scholarship (iRTP) for the M.Res. degree, the International Macquarie University Research Excellence Scholarship (iMQRES) for the Ph.D. degree, the Commonwealth Scientific and Industrial Research Organization (CSIRO) grants on Astronomy and Space Exploration, the Macquarie University Postgraduate Research Fund (PGRF), and the WiMed Travel Support Grants. He was a recipient of the 2016 ICEAA-IEEE APWC Cash Prize and the Macquarie University Deputy Vice-Chancellor Commendation, in 2017. He is the only Researcher in the IEEE Region Ten (Asia-Pacific), who received the Most Prestigious Best Paper Contest of the IEEE Region Ten more than once. He was awarded the Third Prize in 2016, the First Prize in 2018, and the Second Prize in 2019 by the International Competition. He is the highly-commended Finalist and the Winner of the Excellence in Higher Degree Research Award in Science, Technology, Engineering, Mathematics and Medicine (STEMM), Macquarie University, in 2019 and 2020, respectively. In 2020, he was announced as an Outstanding Reviewer of IEEE TRANSACTIONS ON ANTENNAS AND PROPAGATION and received the Research Excellence Award of the Faculty of Science and Engineering, Macquarie University. He also serves as an Associate Editor for the *AEÜ-International Journal of Electronics and Communications* and *Electronics* (MDPI).

SAMAN ZARBAKHSH (Member, IEEE) received the B.Sc. degree in electrical engineering from the Azad university of South Tehran, Tehran, Iran, in 2007, and the M.Sc. degree in electrical engineering from Urmia University, Urmia, Iran, in 2010. He is currently pursuing the Ph.D. degree with the Electrical and Computer Engineering Department, Concordia University, Montreal, QC, Canada. Since 2015, he has been a Researcher and a Teacher Assistant with Concordia University. His current research interests include multifunction antennas, metasurfaces, frequency selective surfaces, and transparent and high gain antennas.

SERIOJA OVIDIU TATU (Senior Member, IEEE) received the B.Sc. degree in radio engineering from Polytechnic University, Bucharest, Romania, in 1989, and the M.Sc.A. and Ph.D. degrees in electrical engineering from École Polytechnique de Montréal, Montreal, QC, Canada, in 2001 and 2004, respectively. He was with Romanian National Telecommunications Company, Rom-Telecom, Bistrita-Nasaud, Romania, where he was an RF Engineer and the Head of the Telecommunications Laboratory, from 1989 to 1993 and the Technical Manager, from 1993 to 1997. He is currently a Full Professor with Énergie Matériaux et Télécommunications, Institut National de Recherche Scientifique, Montreal. He has authored or coauthored more than 175 journal articles and conference papers. His current research interests include microwave/millimeter-wave circuit design and measurement techniques, microwave/millimeter-wave six-port-based transceivers, radar sensors, and imaging systems.

ABDEL-RAZIK SEBAK (Life Fellow, IEEE) received the B.Sc. degree (Hons.) in electrical engineering from Cairo University, Cairo, Egypt, in 1976, the B.Sc. degree in applied mathematics from Ein Shams University, Cairo, in 1978, and the M.Eng. and Ph.D. degrees in electrical engineering from the University of Manitoba, Winnipeg, MB, Canada, in 1982 and 1984, respectively. From 1984 to 1986, he was with Canadian Marconi Company working on the design of microstrip phased array antennas. From 1987 to 2002, he was a Professor with the Department of Electronics and Communication Engineering (ECE), University of Manitoba. He is currently a Professor with the Department of Electrical and Computer Engineering, Concordia University, Montreal, QC, Canada. His research interests include phased array antennas, millimeter-wave antennas and imaging, computational electromagnetics, and interaction of EM waves with engineered materials and bio electromagnetics. He is a member of the Canadian National Committee of International Union of Radio Science (URSI) Commission B. He was a recipient of the University of Manitoba Merit Award for outstanding Teaching and Research, in 2000 and 1992, respectively, the Rh Award for Outstanding Contributions to Scholarship and Research, in 1994, and the Faculty of Engineering Superior, in 1996. He has served as the Chair for the IEEE Canada Awards and Recognition Committee, from 2002 to 2004, and as the Technical Program Chair for the 2002 IEEE CCECE Conference, and the 2006 URSIANTEM Symposium. He is the Technical Program Co-Chair for the 2015 IEEE ICUWB Conference.

OMAR M. RAMAHI (Fellow, IEEE) was born in Jerusalem, Palestine. He received the B.S. degree (Hons.) in mathematics, and electrical and computer engineering from Oregon State University, Corvallis, OR, USA, in 1984, and the Ph.D. degree in electrical and computer engineering from the University of Illinois at Urbana-Champaign, Champaign, IL, USA, in 1990. He then worked with Digital Equipment Corporation (currently HP), where he was a member of the Alpha Server Product Development Group. In 2000, he joined the faculty of the James Clark School of Engineering, University of Maryland, College Park, MD, USA, as an Assistant Professor and later as a tenured Associate Professor. With the University of Maryland, he was also a Faculty Member of the CALCE Electronic Products and Systems Center. He is currently a Professor with the Department of Electrical and Computer Engineering, University of Waterloo, Waterloo, ON, Canada. He has authored or coauthored more than 400 journal articles and conference technical papers on topics related to the electromagnetic phenomena and computational techniques to understand the same. He is the coauthor of the book entitled *EMI/EMC Computational Modeling Handbook* (First edition Norwell, MA, USA: Kluwer, 1998; Second edition New York, NY, USA: Springer-Verlag, 2001; and Japanese edition published in 2005). He was a recipient of the 2004 University of Maryland Pi Tau Sigma Purple Cam Shaft Award. He received the Excellent Paper Award at the 2004 International Symposium on Electromagnetic Compatibility, Sendai, Japan, and the 2010 University of Waterloo Award for Excellence in Graduate Supervision. In 2012, he was a recipient of the IEEE Electromagnetic Compatibility Society Technical Achievement Award.

TAYEB A. DENIDNI (Fellow, IEEE) received the M.Sc. and Ph.D. degrees in electrical engineering from Laval University, Quebec, QC, Canada, in 1990 and 1994, respectively. He was a Professor with the Engineering Department, Université du Quebec at Rimouski, Rimouski, QC, Canada, from 1994 to 2000, where he founded the Telecommunications Laboratory. Since 2000, he has been with the Institut National de la Recherche Scientifique (INRS), Université du Quebec, Montreal, QC, Canada. He found the RF Laboratory, INRS-EM, Montreal. He has extensive experience in antenna design and is leading a large research group consisting of three research scientists, eight Ph.D. students, and two M.Sc. students. His current research interests include reconfigurable antennas using EBG and FSS structures, dielectric resonator antennas, metamaterial antennas, adaptive arrays, switched multi-beam antenna arrays, ultrawideband antennas, microwave, and development for wireless communications systems. He served as an Associate Editor for the IEEE TRANSACTIONS ON ANTENNAS AND PROPAGATION, from 2008 to 2010; and the IEEE ANTENNAS AND WIRELESS PROPAGATION LETTERS, from 2005 to 2007. Since 2015, he has been serving as an Associate Editor for *Electronics Letters* (IET).